Chiral magnetic skyrmions with arbitrary topological charge

Filipp N. Rybakov[1,*] and Nikolai S. Kiselev[2]

[1]*Department of Physics, KTH-Royal Institute of Technology, SE-10691 Stockholm, Sweden*

[2]*Peter Grünberg Institut and Institute for Advanced Simulation, Forschungszentrum Jülich and JARA, D-52425 Jülich, Germany*

(Received 4 June 2018; revised manuscript received 6 October 2018; published 28 February 2019)

We show that continuous and spin-lattice models of chiral ferro- and antiferromagnets provide the existence of an infinite number of stable soliton solutions of any integer topological charge. A detailed description of the morphology of new skyrmions and the corresponding energy dependencies are provided. The considered model is general, and is expected to predict a plethora of particlelike states which may occur in various chiral magnets including ultrathin films, e.g., PdFe/Ir(111), rhombohedral GaV_4S_8 semiconductor, B20-type alloys as $Mn_{1-x}Fe_xGe$, $Mn_{1-x}Fe_xSi$, $Fe_{1-x}Co_xSi$, Cu_2OSeO_3, and acentric tetragonal Heusler compounds.

DOI: 10.1103/PhysRevB.99.064437

I. INTRODUCTION

The existence of stable localized magnetic vortices in the presence of so-called chiral interactions was predicted in 1989 [1]. Nowadays, it is common to use the term *chiral magnetic skyrmions* for these vortices. In contrast to baby skyrmions [2,3], and superconducting skyrmions [4], chiral magnetic skyrmions are not related to the model of baryons proposed by Skyrme [5,6] neither explicitly nor implicitly [7]. Similarly to the aforementioned skyrmions, these magnetic vortices can be characterized by a nonzero topological charge Q. The corresponding micromagnetic Hamiltonian contains competing terms of different powers of spatial derivatives with respect to the order parameter mimicking the Skyrme mechanism of stabilization [8]. The presence of competing terms highlights the model of a chiral magnet among many other models in nonlinear physics where the Hobart-Derrick theorem forbids the existence of stable localized solutions [9].

The research in this field has gotten a powerful impetus after the direct observation of magnetic skyrmions in cubic chiral magnets of B20 type employing transmission electron microscopy [10]. Later, the existence of magnetic skyrmions has been confirmed in many other materials [11–15]. Several new phenomena have been reported recently: different approaches for the nucleation of magnetic skyrmions [11,16], electric current induced motion of skyrmions [17], and attractive and repulsive interskyrmion interactions [18,19]. The possible utilization of magnetic skyrmions in spintronic devices is also under intensive study [20–25].

A fundamental question concerning the diversity of possible skyrmion solutions remains unaddressed in the literature despite the large number of experimental and theoretical works published within the last decade. Indeed, some of the two-dimensional (2D) models, such as baby Skyrme [2,3] and isotropic ferromagnet [26], possess a wide variety of solutions with an arbitrary integer Q. Some solutions with $|Q| > 1$ are also known [27–30] in the model of frustrated magnet with competing exchange interactions [31]. However, in the frame of an underlying model of chiral magnet, it was assumed that the diversity of skyrmions is limited to topological charge $Q = \pm 1$ [32–34]. This underlying model [1,35,36] contains only three energy terms: the exchange interaction, chiral Dzyaloshinskii-Moriya interaction (DMI) [37,38], and potential term. The latter one represents the interaction with an external magnetic field $\mathbf{B}_{\text{ext}}$ and/or magnetic anisotropy, meaning the presence of energetically preferable directions for magnetization vector $\mathbf{M}(\mathbf{r})$.

First, the static skyrmion solution with $Q = -1$ has been reported in Ref. [1]. There is a generalization of this solutions nowadays known as Bogdanov-Hubert $k\pi$ vortices [39] characterized by alternating $Q = -1$ and $Q = 0$ for odd and even k, respectively. For convenience, we employ the term π *skyrmion* [40] referring to 1π vortex with $Q = -1$ and the term *skyrmionium* [41,42] for 2π vortex with $Q = 0$.

Following the classification of skyrmion solutions given in Ref. [1], one can show (see also the discussion in Ref. [43]) that by applying trivial operations of reflection and rotation to the magnetization vectors, the solutions corresponding to the different type of crystal symmetries can be always mutually transformed one into another. Thus, these solutions belong to the same class. An important consequence of such classification is that stable magnetic textures recently discovered in tetragonal Heusler alloy [14] and named "antiskyrmion" in fact belongs to the same class of π-skyrmion solutions.

In the work by Zhang *et al.* [44] it was concluded that in a conventional model of a chiral magnet a skyrmion with $|Q| \geqslant 2$ cannot exist as a static stable solution. The authors observed a skyrmion with $|Q| = 2$ in numerical simulations as a nonequilibrium dynamical object only. Moreover, Koshibae and Nagaosa argued [45] that in a conventional model of a chiral magnet even the coexistence of stable skyrmion solutions with $Q = -1$ and $Q = 1$ is impossible.

In this paper, it is shown that in fact, a conventional model of chiral magnet possesses an infinite set of skyrmion solutions with different value and sign of topological charge and diverse morphology.

*f.n.rybakov@gmail.com

II. MODEL

The energy functional for the continuous two-dimensional model of a chiral magnet can be written in the following form [1]:

$$E = \int \left(\mathcal{A} \sum_i (\nabla n_i)^2 + \mathcal{D}\, w(\mathbf{n}) + U(n_z) \right) t\, dx\, dy, \quad (1)$$

where $\mathbf{n} \equiv \mathbf{n}(\mathbf{r})$ is a continuous unit vector field ($n_x^2 + n_y^2 + n_z^2 = 1$) determining the direction of the magnetization $\mathbf{n} = \mathbf{M}/M_s$ and $\mathcal{A}$ and $\mathcal{D}$ are the micromagnetic constants for exchange and DMI, respectively. t represents the layer thickness. The last term in (1) is the potential term, which consists of the Zeeman energy: $U_Z = B_{ext}\, M_s\, (1 - n_z)$, and/or the energy density of uniaxial anisotropy $U_a = K\,(1 - n_z^2)$. The DMI term $w(\mathbf{n})$ represents a linear combination of Lifshitz invariants:

$$\Lambda_{ij}^{(k)} = n_i \frac{\partial n_j}{\partial r_k} - n_j \frac{\partial n_i}{\partial r_k},$$

which in turn is defined by the underlying symmetry of the crystal.

The results presented below are valid for a very wide class of chiral magnets of various lattice symmetries: for the systems with Néel-type chiral modulations [11,13,46] where $w(\mathbf{n}) = \Lambda_{xz}^{(x)} + \Lambda_{yz}^{(y)}$, for the tetragonal compounds of D_{2d} symmetry [14] with $w(\mathbf{n}) = \Lambda_{zy}^{(x)} + \Lambda_{zx}^{(y)}$, and for the crystals with bulk-type DMI and Bloch-type chiral modulations [10,47,48] where $w(\mathbf{n}) = \Lambda_{zy}^{(x)} + \Lambda_{xz}^{(y)} + \Lambda_{yx}^{(z)} = \mathbf{n} \cdot (\nabla \times \mathbf{n})$. For systems with bulk-type DMI, e.g., B20-type crystals, the solutions discussed below should be considered as a new kind of skyrmion tubes (or strings) that were previously known only for the case of a π skyrmion [19,49–53]. Note, when the term $\Lambda_{yx}^{(z)}$ play a significant role [49,54] one should solve a three-dimensional problem.

For the case of magnetic multilayers and heterostructures with interface-induced DMI [55], the demonstration of the stability of the solutions displayed further might suggest that isolated π domains (also known as bubble skyrmions) [56–59] belong to the category of chiral skyrmions. In the eventuality where such a scenario fails, one can conclude that the magnetic dipole-dipole interaction represents the core mechanism for the stabilization of those domains. This in turn indicates that such objects are magnetic bubbles [60] rather than chiral skyrmions.

For convenience, all parameters such as the lengths, the value of the external magnetic field, and the energy are given in relative dimensionless units of: the equilibrium period of helical spin spiral [61,62] $L_D = 4\pi\mathcal{A}/|\mathcal{D}|$, the critical field of the cone spiral transition into saturated state [62] $B_D = \mathcal{D}^2/(2M_s\mathcal{A})$, and the energy $E_0 = 2\mathcal{A}t$. Thereby, only two dimensionless parameters which define the state of the system are required:

$$h = B_{ext}/B_D, \quad u = K/(M_s B_D).$$

III. TOPOLOGICAL CHARGE

The localized solutions are the excitations on the homogeneous background, in other words $\mathbf{n}(\mathbf{r}) \to \mathbf{n}_0$ for $|\mathbf{r}| \to \infty$. Thus, the domain of the definition of the order parameter $\mathbf{n}(\mathbf{r})$ can be mapped to a sphere which can be associated with a Riemann sphere ($\mathbb{R}^2 \cup \{\infty\} \leftrightarrow \mathbb{S}^2$). The space of the order parameter $\mathbf{n}$ is in turn a sphere $\mathbb{S}^2_{spin}$. The map $\mathbb{S}^2 \to \mathbb{S}^2_{spin}$ leads to an homotopy classification of localized solutions in 2D with topological invariants related to an integer index

$$Q = \frac{1}{4\pi} \int [\mathbf{n} \cdot (\partial_x \mathbf{n} \times \partial_y \mathbf{n})] dx dy. \quad (2)$$

For topologically nontrivial textures $Q \neq 0$ a continuous transformation into a homogeneous state $\mathbf{n}(\mathbf{r}) = \mathbf{n}_0$ is impossible. We follow the sign convention for a topological charge given in Ref. [63], and for definiteness we assume the polarity with $\mathbf{n}_0 = (0, 0, 1)$.

Note, Eq. (2) often represents a useful quantity for the estimation of the number of π skyrmions in the clusters appearing due to the geometrical confinement of the sample [64,65] or under the pressure of surrounding nonuniform helical phase [66], as well as π skyrmions under the impact of spatially varying external stimuli [67] or different pinning effects [68]. The topological charge $|Q|$ of these clusters can be greater than one. However, it is essential to distinguish between a cluster of particles and a single skyrmion with topological charge Q. This aspect can be easily explained by analogy to the Skyrme model for atomic nuclei. In this model the topological charge B corresponds to the baryon number of the nuclei. For instance, the helium-4 atom has B = 4 and its nucleus is a single skyrmion, while deuterium molecule D_2 has the same B = 4 but includes two nuclei and thus represents the cluster of two skyrmions.

IV. RESULTS AND DISCUSSIONS

The earlier stable solution was found for π skyrmion with an energy below [1] and above [69] the saturated state, which represents only a single example of the vast variety of topologically nontrivial solutions, see Fig. 1. For the case of $u = 0$ and high magnetic fields $h \geqslant 2$ it was shown [63] that π skyrmion is energetically most favorable among all other hypothetical configurations with $Q \neq 0$. It will be shown below that π skyrmion and skyrmionium with $Q = 0$ are the key elements or "building blocks" of which the whole variety of other skyrmions is "constructed."

One may highlight two main reasons why stable skyrmion solutions with $Q < -1$ and $Q > 0$ have been overlooked earlier: (i) the interparticle repulsion of π skyrmions [8] and (ii) an extremely limited set of axisymmetric critical points [70] of the Hamiltonian (1). Both effects obstruct the merging process of π skyrmions into one particle, and instead result in them moving apart which is the so-called dichotomy [71]. Consequently, naive attempts to stabilize $Q = -N$ skyrmion by using N isolated π skyrmions as an initial guess cannot lead to the nucleation of a big single skyrmion in numerical simulation.

To find energetically stable solutions, we performed a direct energy minimization of the functional (1) based on a nonlinear conjugate gradient method which in our implementation has been massively parallelized and optimized for NVIDIA CUDA architecture. We used a finite-difference discretization scheme of the fourth order with a meshes varying

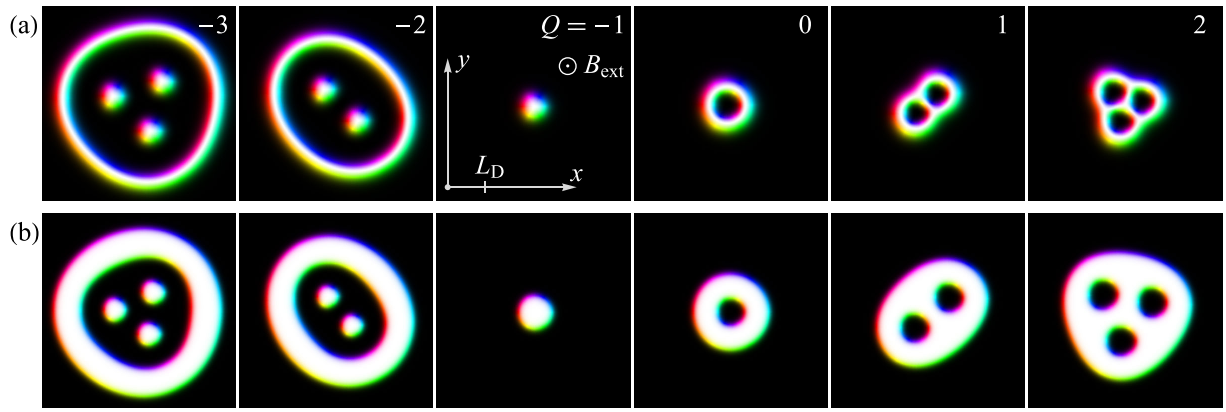

FIG. 1. Morphology of stable chiral skyrmions with topological charges $Q = -3, -2, \ldots, 2$. Top row of images (a) corresponds to zero magnetocrystalline anisotropy ($u = 0$) in external magnetic field applied perpendicular to the plane $h = 0.65$. Bottom row of images (b) corresponds to the case of uniaxial anisotropy $u = 1.3$ and zero external field $h = 0$. All images are given in the same scale. Colors encode the direction of the **n** vectors according to a standard scheme [54]: black and white denote up and down spins, respectively, and red-green-blue reflect the azimuthal angle with respect to x axis.

from 640^2 to 5120^2 nodes (see Appendix A). The values of the variables $\mathcal{A}$ and $\mathcal{D}$ have been chosen such that the parameter L_D equals 52 internode distances.

Supplementary movies [72] illustrate the process of crafting the initial states for different anticipated morphologies of skyrmion solutions and the energy minimization process (see Appendix B for details).

To obtain a $Q < -1$ skyrmion, we put $N_{cores} = |Q|$ number of π skyrmions inside a "sack" representing a closed 2π domain wall, i.e., skyrmionium which has topological charge $Q = 0$ (see Fig. 1). This closed domain wall plays the role of the shell of the skyrmion and has a tendency to shrink down to the equilibrium size of skyrmionium. Interparticle repulsion of π skyrmions in turn prevent such shrinking. Similar to the effect of surface tension, the balance of external and internal pressures results in the stability of this spin texture. For a skyrmion with $Q > 0$ the role of a sack or a shell is played by a closed π domain wall which possesses a nonzero topological charge $Q = -1$ as a π skyrmion. The domain within the closed loop has magnetization opposite to the surrounding ferromagnetic background. Due to the opposite polarity, each π vortex inside such a sack has a self-topological charge $Q = 1$. In Fig. 1 see $Q = 1$ and 2, they look like "holes" inside the white domains. As a result, the total topological charge (2) gives $Q = (N_{cores} - 1)$, where the amount of cores is equal to the number of holes. We found solutions with absolute values of Q equal to units, tens, hundreds, and even thousands (see Appendix C for details). Thereby there is every reason to expect that Q can be equal to any arbitrary large integer number.

The dependence of the skyrmion energy as a function on its topological charge is found to be well approximated by a piecewise linear function for small $|Q|$, while some points slightly deviate from the linear law (Figs. 2 and 3). Note, the linear law dependence $E(Q)$ is known to be a good approximation in the baby Skyrme model [2,3], while for an isotropic ferromagnet model [26] the relation is strictly linear. Our analysis shows (see Appendix C) that the curves $E_{aspt} = E_0\,(\alpha_{(\pm)} N_{cores} + \beta_{(\pm)} \sqrt{N_{cores}})$ are good candidates for the true asymptotics when $Q \to \pm\infty$. Moreover, a detailed numerical analysis with a high precision confirm the equality $\alpha_{(-)} = E_{Q=-1}/E_0$ (for details see Appendix C).

Let us first consider the case where $u = 0$ (Fig. 2) and some arbitrary chosen h above the field of the elliptical instability [73] and below the field of the thermodynamic stability of π skyrmion, $E_{Q=-1} < 0$ [74]. The right branch of the "spectrum" for $Q \geqslant -1$, Fig. 2, increases monotonically with Q. In contrast to that the left branch of the spectrum ($Q < -1$) displays the opposite behavior and the energy decreases with $|Q|$. This feature reflects the fact that the global energy minimum corresponds to a hexagonal lattice of π skyrmions [74], and the big skyrmions $Q \ll -1$ on the left branch of the spectrum form a kind of lattice inside their shells (see Appendix C).

Significantly, the set of the solutions contains also states with higher energies. In Fig. 2 we have shown only the

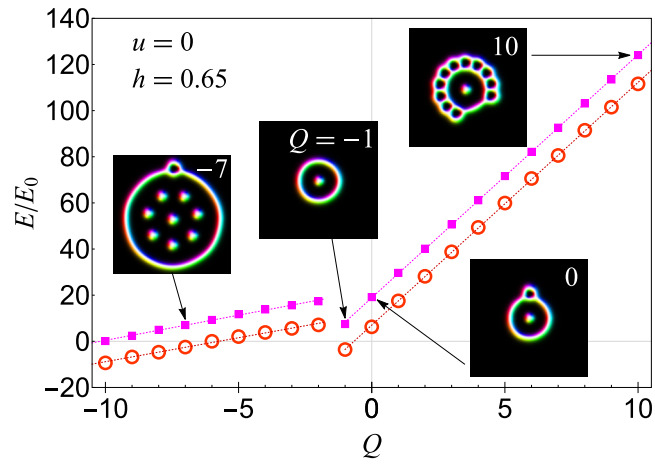

FIG. 2. The energy of skyrmions E as function of topological charge Q for the case of a magnet without magnetocrystalline anisotropy $u = 0$. Open circles are the lowest energy solutions for each particular Q, and solid squares are solutions with higher energies but nearest to the lowest energy state. The dotted lines are linear fits for corresponding sets of points.

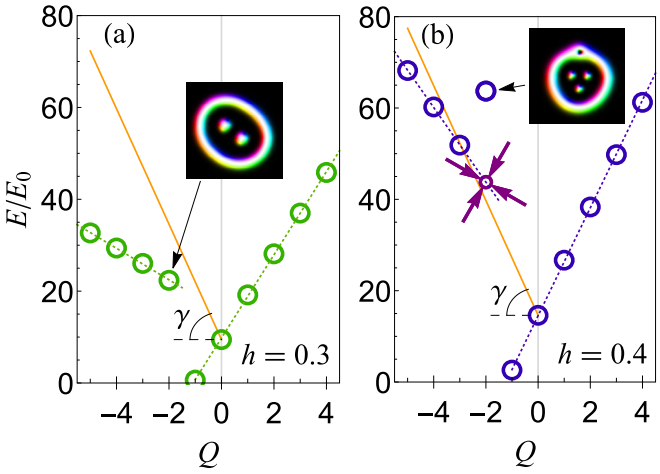

FIG. 3. The energy of skyrmions E as function of topological charge Q for the case of uniaxial anisotropy $u = 0.65$ in external magnetic field $h = 0.3$ (a) and $h = 0.4$ (b). The slope of the solid line is defined as $\tan(\gamma) = 4\pi$. The point marked by four thick arrows in (b) corresponds to the solution expected from the linear fit of the energy dependence and with morphology shown in the inset in (a), but precise calculations shows instability of expected skyrmion. The morphology of stable and energetically most favorable skyrmion with $Q = -2$ is shown in the inset.

energies of those states which corresponds to the smallest energy shift. Some of those solutions are shown in the inset. Note that $Q = -1$ skyrmion in the inset of Fig. 2 corresponds to earlier known solution of 3π vortex [39]. We believe that the set of the solutions corresponding to the lowest energy states, open circles in Fig. 2, represent true minimizers in the corresponding topological sectors.

For the case of a nonzero out-of-plane uniaxial anisotropy, Fig. 3, we used the value $u = 0.65$, which according to Ref. [46], corresponds to the bilayer of PdFe on an Ir(111) single crystal substrate. We performed calculations for two values of h for which $E_{Q=-1} > 0$. Both branches of the spectrum (Fig. 3) now demonstrate the same trend. Above certain values of h, the energy of some points of the left branch of the spectrum become higher than the critical Dirichlet energy [26,75] shifted up on the corresponding energy of skyrmionium, see solid line in Figs. 3(a) and 3(b). This means that the corresponding expected solutions become unstable, see for instance the point marked with four arrows in Fig. 3(b). Such instability can be explained as follows: The pressure from the shell becomes too high and leads to the shrinking [75] of the internal π skyrmions. This may result in blow-up behavior of the solutions [76] with an increasing magnetic field. From that one may conclude that in the case of such a critical phenomena, a certain solution of higher energy branch becomes the minimizer for corresponding Q, see inset in Fig. 3(b).

The above discussed solutions are not restricted to the continuum model and can be generalized to spin-lattice models of chiral ferro- and antiferromagnet. In Appendix D we present solutions for such models, and discuss their morphology and key features.

V. CONCLUSIONS

In conclusion, we have shown that the standard micromagnetic model with chiral Dzyaloshinskii-Moriya interaction allows the existence of chiral magnetic skyrmions with any integer topological charge. The morphology of the new solutions with $Q < -1$ and $Q > 0$ are described in detail, and are found to be sufficiently different from the systems where the interparticle attraction naturally leads to the formation of clusters [4,77–79]. The energies of skyrmions with a high topological charge are found to be comparable to each other and controllable by an external magnetic field. The latter suggests that the direct observation of a large variety of new particlelike states presented here should be accessible in experiment. We suppose that the nucleation of new skyrmions can possibly be realized with a scanning tunneling microscope equipped with the magnetic tip of a special shape [80] or by means of a time-dependent external magnetic field or a current induced spin torque effect in geometrically confined systems. The stabilized solitons can be considered as information bit carriers in a skyrmion racetrack memory and may extend a newly proposed concept of "two particles" for binary data encoding, as skyrmion-bobber chains in cubic chiral magnets [24], or sequences of skyrmions and antiskyrmions in spatially anisotropic ultrathin films [43].

Finally, one has to emphasize that the found solutions with $|Q| > 1$ are natural high charge skyrmions for the corresponding model, while the $Q = 1$ solution presented in this work should be considered as an actual antiparticle for π skyrmion.

During the review process, we became aware of an independent work [81] where authors report on similar theoretical findings and provide experimental evidence of so-called "skyrmion bags" observed in liquid crystals which mimics the skyrmions with high topological charge addressed in this work.

ACKNOWLEDGMENTS

The authors thank C. B. Muratov, E. Babaev, S. Komineas, J. Bouaziz, and C. Melcher for useful discussions of results. The work of F.N.R. was supported by the Swedish Research Council Grant No. 642-2013-7837, by Göran Gustafsson Foundation for Research in Natural Sciences and Medicine, and by the "Roland Gustafssons Stiftelse för teoretisk fysik." The work of N.S.K. was supported by Deutsche Forschungsgemeinschaft (DFG) via SPP 2137 "Skyrmionics" Grant No. KI 2078/1-1.

APPENDIX A: ACCURACY OF FINITE DIFFERENCE SCHEMES

In this Appendix we discuss the accuracy of the numerical methods employed to calculate various skyrmionic solutions with different topological charge and morphology presented in the main text of the paper as well as in the Appendixes. We compared the results of energy minimization obtained by our method with the second-order finite difference schemes implemented in most open-source software for micromagnetic simulations such as MuMax3 [82]. A high accuracy numerical scheme used in our work is essential for the study of a number

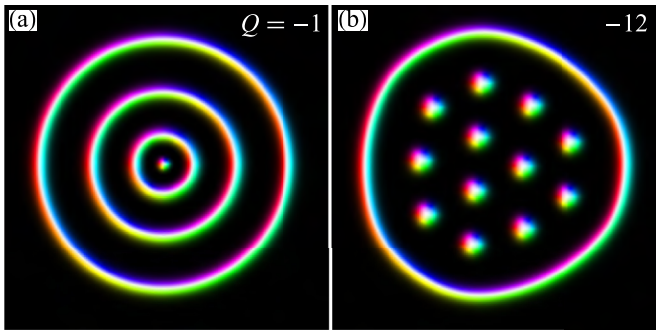

FIG. 4. Example of two solitons of nearly identical size but different morphology and topological charge: axisymmetric 7π vortex [39] with $Q = -1$ (a) and skyrmion with $Q = -12$ (b). Both solutions corresponds to the case $u = 0$, $h = 0.65$. Both images are given in the same scale. The color code is identical to that one used in Figs. 1–3 in the main text.

of aspects: the stability of the solutions close to blow-up, energy of skyrmions with extremely big topological charge, etc. Moreover, we provide additional calculations with a very high accuracy reducing the relative error in energy down to 10^{-6}. These calculations can be taken as benchmarks and compared with the outputs provided by other methods. Such high accuracy can be achieved only for axisymmetric solutions [39], where the problem can be reduced to an ordinary differential equation. An example of axisymmetric solution is depicted in Fig. 4(a). Furthermore, we show a nonaxisymmetric solution of a comparable size with a more complex morphology in Fig. 4(b). The results obtained with our precise method for axisymmetric solutions can be taken as a reference to define a threshold for more general solutions with lower symmetries.

The Hamiltonian (1) in the main text can be rewritten in dimensionless units:

$$\mathcal{E} = \frac{E}{E_0} = \int \left(\frac{1}{2} \sum_i (\nabla n_i)^2 + 2\pi\, w(\mathbf{n}) + 4\pi^2\, u\,(1 - n_z{}^2) + 4\pi^2\, h\,(1 - n_z) \right) d\mathrm{x} d\mathrm{y}, \tag{A1}$$

where $\mathrm{x} = x/L_\mathrm{D}$, $\mathrm{y} = y/L_\mathrm{D}$, E_0, and L_D are defined in the main text.

In the case of axisymmetric solitons [1,39], the solution of the problem (A1) can be reduced to a second-order nonlinear nonautonomous ordinary differential equation:

$$\underbrace{\frac{d^2\theta}{d\rho^2} + \frac{1}{\rho}\frac{d\theta}{d\rho} - \frac{1}{\rho^2}\sin(\theta)\cos(\theta)}_{\text{exchange}} + \underbrace{\frac{4\pi}{\rho}\sin(\theta)^2}_{\text{DMI}} - \underbrace{4\pi^2 u \sin(2\theta)}_{\text{uniax. anis.}} - \underbrace{4\pi^2 h \sin(\theta)}_{\text{Zeeman}} = 0, \tag{A2}$$

where θ is the polar angle of magnetization vector, i.e., $n_z = \cos(\theta)$, and ρ is the radial coordinate.

The soliton solutions of Eq. (A2) are exponentially localized [83], even in the absence of the DMI contribution [84]. The true asymptotic of such solutions behaves as a Macdonald function [85,86]:

$$\theta(\rho) \sim \frac{1}{\sqrt{\rho}} \exp(-2\pi\sqrt{2u + h}\,\rho) \quad \text{for} \quad \rho \to \infty. \tag{A3}$$

This exponential decay of the solution renders the error introduced by the finite-size domain negligible. The discretization scheme plays a major role in the achievement of the required high accuracy. We are particularly interested in the behavior of the error with respect to the size and morphology of the skyrmion texture. A higher accuracy can be achieved for the one-dimensional (1D) problem (A2) since our solution θ depends only on ρ. Contrary to the 2D case the solution of such a 1D problem does not require considerable computational efforts, and high accuracy results can be obtained on very dense meshes with internode distance $\sim$0.001 (about a 1000 nodes per L_D). Such high-accuracy solutions then can be used as benchmarks to verify the accuracy of other methods.

Equation (A2) can be solved numerically by means of explicit integration relying of the Runge-Kutta method [39]. Assuming $\theta(0) = k\pi$, where k is an integer, the proper value of the parameter $\theta'(0) = d\theta/d\rho|_{\rho=0}$ can be found by the shooting method. Thus, the solution is uniquely "encoded" in a single number θ' and every overshooting/undershooting should lead to a distortions of the $\theta(\rho)$ profile which is expected to decrease monotonically to zero as $\rho \to \infty$. This property of the explicit integration method can be used to verify the correctness of the results obtained with other methods. In particular, we found the solution of the 1D problem (A2) by the unconstrained nonlinear conjugate gradient (NCG) minimization method for corresponding Hamiltonian:

$$\mathcal{E}_\mathrm{1D} = 2\pi \int_0^\infty \left[\frac{1}{2}\left(\frac{d\theta}{d\rho}\right)^2 + \frac{1}{2\rho^2}\sin(\theta)^2 + 2\pi\frac{d\theta}{d\rho} + \frac{\pi}{\rho}\sin(2\theta) + 4\pi^2 u \sin(\theta)^2 + 4\pi^2 h[1 - \cos(\theta)] \right] \rho\, d\rho. \tag{A4}$$

A very large simulation domain was used $0 \leqslant \rho \leqslant 10$ and very small internode distance $\Delta\rho = 0.005$. The values at the boundaries $\theta(0)$ and $\theta(10)$ was fixed to $k\pi$ and 0, respectively. A finite-difference scheme of the fourth order of accuracy was designed assuming that θ_i and its spatial derivative θ_i' at each node i are independent variables. According to our estimates the relative error in the calculation of the energy marked in bold font shown in the Table I does not exceed

TABLE I. The energies of several solitons calculated by different methods.

				Energy $\mathcal{E}$					
Texture type	Q	u	h	MuMax3 \ 2 $\Delta s = 1/52$	Atlas \ 2 1/52	Atlas \ 2 1/104	Atlas \ 4 1/52	1D \ 4 1/200	$\theta'(0)$
Axisymmetric skyrmion	−1	0	0.65	−3.522	−3.527	−3.556	−3.565	**−3.56497**	−4.553561
2π vortex (skyrmionium)	0	0	0.65	6.476	6.472	6.322	6.274	**6.27244**	−2.424450
7π vortex	−1	0	0.65	55.45	55.46	53.63	53.02	**53.0071**	−8.847806
Skyrmion	+1	0	0.65	17.85	17.79	17.59	17.52	not applicable	not applicable
Skyrmion	−3	0	0.65	6.466	6.462	5.808	5.595	not applicable	not applicable
Skyrmion	−12	0	0.65	−12.54	−12.54	−13.91	−14.37	not applicable	not applicable
Axisymmetric skyrmion	−1	0.65	0.3	0.673	0.673	0.6341	0.6220	**0.621763**	−3.012659
Axisymmetric skyrmion	−1	0.65	0.4	2.666	2.666	2.628	2.617	**2.61621**	−4.561866

10^{-6}. For additional verification we used the value $\theta'_{i=0}$ (the value in the first node for which $\rho = 0$) from the found solution as an initial input value $\theta'(0)$ for the integration with the fourth-order Runge-Kutta method (RK4). We used the integration step $\Delta\rho = 10^{-7}$ and found during a further shooting procedure that at least the first six significant digits of $\theta'_{i=0}$ are accurate. All calculations for the 1D problem were carried out in double-precision format (64 bits) for floating-point operations.

The contributions of exchange and Dzyaloshinskii-Moriya interaction terms at each (i, j)th node with coordinates $(\mathrm{x}, \mathrm{y}) = (i\,\Delta s, j\,\Delta s)$ in 2D mesh are approximated using the values of the unit vector field in eight neighboring nodes with $(\mathrm{x}\pm\Delta s, \mathrm{y}\pm\Delta s)$ and $(\mathrm{x}\pm2\Delta s, \mathrm{y}\pm2\Delta s)$, where Δs is the internode distance. The corresponding energy contributions represent the products of the **n**-vector projections at each node and its eight neighbor nodes multiplied by specific factors, see for instance Ref. [87] and the Supplemental Material in Ref. [50]. For testing purposes we have also implemented in our code the conventional second-order finite difference scheme. For direct energy minimization, we used the constrained NCG algorithm where the constraint $\mathbf{n}^2 = 1$ is naturally satisfied because of using the atlas for the manifold corresponding to the space of the order parameter. The manifold itself represents a two-dimensional sphere $\mathbb{S}^2_{\mathrm{spin}}$ while the atlas is composed of two coordinate charts each of which corresponds to stereographic projection from one of two poles of the sphere. Here we refer to this advanced numerical scheme as "atlas." Conceptually such a scheme is similar to the idea of describing the macrospin in the frame of stereographic projections with the ability to switch between projections from both poles, presented in Ref. [88]. The key feature of the atlas scheme is that each individual spin is defined in one of two coordinate charts independently on other spins. A more detailed description of the method and criteria for switching between charts for individual spins can be found in the Supplemental Material in Ref. [51]. Note, most of the floating-point operations in our code have been implemented in single-precision format (32 bits). This allows us to reach high performance on GPU.

In Table I we present the comparison of the results obtained with MuMax3 where a second order finite-difference scheme is implemented [82] (the script is provided in [72]), different implementation of the atlas method with second order (see "Atlas \ 2" columns with $\Delta s = 1/52$ and more dense mesh with $\Delta s = 1/104$), fourth order finite-difference scheme (see "Atlas \ 4" column), and one-dimensional approach (see "1D \ 4" column). It is seen that the method chosen in the current work provides the best accuracy with an error lower than 0.04% as for $Q = -1$ skyrmions as for more complex textures. In contrast, the second-order finite-difference scheme widely used in micromagnetic software shows significant error of about 8% for the same relatively dense mesh. Increasing twice the mesh density in each of the dimensions reduces this error only by factor 4 as expected for the second-order scheme. A simple estimate suggests that one requires to increase the mesh density 14 times more in each dimension to provide an accuracy comparable to our fourth-order scheme. Finally, it worth mentioning that the calculations for the textures with characteristic size of $\sim 10L_{\mathrm{D}}$ (see for instance Fig. 4) with second-order discretization scheme on the meshes with $\Delta s \sim 0.01L_{\mathrm{D}}$ provides an absolute error in energy calculations higher than value of E_0. Therefore, for quantitative analysis of such larger textures the second-order discretization scheme becomes unreliable.

APPENDIX B: REAL-TIME SIMULATIONS

One of the key features implemented in our code is the graphic user interface with an interactive regime allowing the *in situ* control of the magnetic configurations as well as an easy way to construct a large variety of initial states. In particular, when being in the interactive regime, one can flip the spins inside a certain area under the mouse pointer. This option provides an efficient approach for construction of complex initial configurations composed of domains with a magnetization pointed either up or down. After a certain number of iterations of the energy minimization routine, the initial configuration converges to one of the nearest energy minimum. Beside the calculation of standard termination criteria [89] one can also perform an *in situ* examination of the stability by introducing small excitations and perturbations to the simulated spin texture.

In order to emphasize the isomorphism of systems with different Lifshitz invariants, we prepared three distinct movies illustrating the case of C_{nv}, $D_{2\mathrm{d}}$, and D_{n} symmetries. The Supplementary Video [72] contains three files: "movie1_Cnv.mp4," "movie2_D2d.mp4," and "movie3_Dn.mp4."

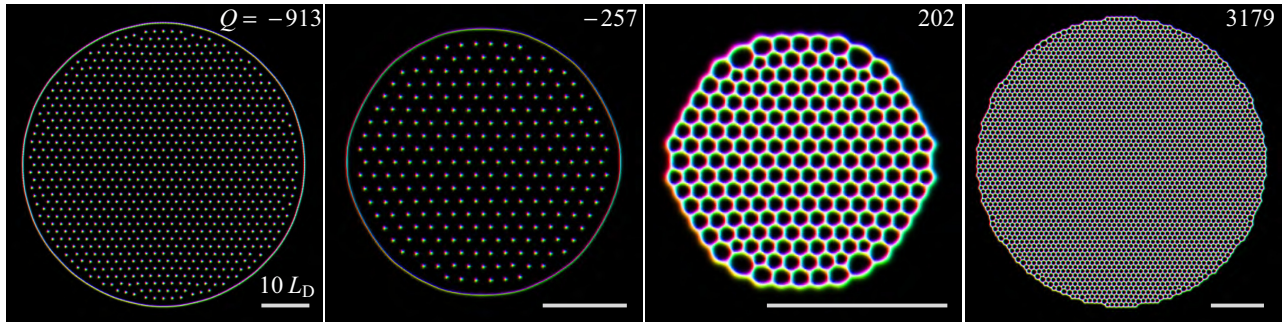

FIG. 5. Morphology of stable chiral skyrmions with high topological charges in the case of magnetic field applied perpendicular to the plane $h = 0.65$ and zero magnetocrystalline anisotropy $u = 0$. Note, the scale is different for all figures.

APPENDIX C: BIG AND EXTREMELY BIG SKYRMIONS

It the case of $|Q| \gg 1$, the kernel of the skyrmion, its major internal part, consists of tightly packed cores representing π vortices. The shell of such heavy skyrmions which represents a π or 2π domain wall for positive and negative Q, respectively, occupies a relatively small area along the outer perimeter, see Fig. 5. When increasing the number of cores (N_{cores}) the structure of the skyrmion kernel becomes more regular while the area engaged by the kernel increases proportionally to N_{cores}. As a result, the energy of the skyrmion kernel tends to be proportional to N_{cores} while contribution from the boundary is proportional to the perimeter of the skyrmion and is proportional to $\sqrt{N_{\text{cores}}}$. Thereby, the asymptotic behavior of the energy of the skyrmions with increasing $|Q|$ should have the following form:

$$\frac{E_{\text{aspt}}}{E_0} = \begin{cases} \alpha_{(-)}|Q| + \beta_{(-)}\sqrt{|Q|} & (Q \ll -1), \\ \alpha_{(+)}(Q+1) + \beta_{(+)}\sqrt{Q+1} & (Q \gg 1), \end{cases} \tag{C1}$$

where $\alpha_{(\pm)}$, $\beta_{(\pm)}$ are the constants which depend only on u and h.

For the careful verification of (C1), we first calculated ten skyrmions (five for negative Q and five for positive Q) with relatively high topological charges in the range $100 \leqslant |Q| \leqslant 300$ [see empty circles in Figs. 6(a) and 6(c)]. Then assuming that such values of $|Q|$ are sufficiently large for the energy to be slightly different from the asymptote fitted with (C1) we obtain the following fitting parameters: $\alpha_{(-)} = -3.552$, $\beta_{(-)} = 7.663$, $\alpha_{(+)} = 9.885$, $\beta_{(+)} = 2.308$. The dependencies corresponding to (C1) are represented as solid curves in Figs. 6(a)–6(c). Finally, in order to verify the expected asymptotic behavior, we have calculated the energies corresponding to the skyrmions with extremely high $|Q|$. As seen from Figs. 6(a) and 6(c), the agreement is excellent.

To emphasize the deviation of $E(Q)$ from the linear dependence, we plotted results of the linear fit with the same points assuming $E \approx c_1|Q| + c_2$, see the dashed lines in Figs. 6(a) and 6(c).

Despite the fact that for large $|Q|$, the cores form a triangular lattice, the corresponding unit cell is different from the one of the skyrmion lattice phase also known as a *skyrmion crystal*. In particular, the interskyrmion distances for an equilibrium skyrmion lattice is different from the intercores distance found in the kernels of big skyrmions. In the case of the equilibrium skyrmion lattice, the particles are packed in such a way that the average energy density is minimized, while the number of particles is assumed to be unlimited in an infinite space. In contrast, the packing in the kernel of a big skyrmion minimizes the total energy for a fixed number of cores inside a limited size domain.

In the case of negative Q, if $|Q|$ increases, then the pressure inside the sack decreases together with the curvature of the shell. Thereby, the stress of the internal lattice should tend to zero as $Q \to -\infty$. For such a limiting case this lattice can be regarded in a first approximation as a set of individual noninteracting $Q = -1$ skyrmions, which means that $\alpha_{(-)}$ is equal to $E_{Q=-1}/E_0$. Our calculation gives $E_{Q=-1}/E_0 = -3.565$ (Table I). The corresponding discrepancy is only 0.4% mostly due to the fact that the coefficients for the asymptote are obtained for a finite value of $|Q|$. For the case of uniaxial anisotropy ($u = 0.65$, $h = 0.3$), following the same procedure we found $\alpha_{(-)} = 0.627$. The corresponding energy $E_{Q=-1}/E_0 = 0.622$ (Table I).

APPENDIX D: SKYRMIONS IN LATTICE MODELS

1. Chiral ferromagnet

The results presented in this work which employs a high accuracy method for the quantitative analysis of continuous solutions remain valid in the discrete limit of classical spins on lattice. In addition to that, our results are also validated by the discrete approach for systems where the continuum approach (1) is unsuitable. For illustration, we consider a standard spin lattice model of a chiral magnet [90,91]:

$$\mathcal{H} = -J \sum_{\langle ij\rangle, i>j} \mathbf{n}_i \cdot \mathbf{n}_j - \sum_{\langle ij\rangle, i>j} \mathbf{D}_{ij} \cdot [\mathbf{n}_i \times \mathbf{n}_j] - K_{\text{u}} \sum_i n_{i,\text{z}}^2 - \mu_{\text{s}} \mathbf{B}_{\text{ext}} \sum_i \mathbf{n}_i, \tag{D1}$$

where J is the exchange coupling constant, and μ_{s} is the magnetic moment of each spin. The unit vector $\mathbf{n}_i$ defines the orientation of the spin at site i. The notation $\langle ij\rangle, i > j$ denotes that the summation runs over each nearest-neighbor pair once. We assumed that each Dzyaloshinskii-Moriya pseudovector $\mathbf{D}_{ij}$ is perpendicular to the bond between sites i and j and lies in the (xy) plane. The modulus of vector $D = |\mathbf{D}_{ij}|$ is assumed to be fixed for all interacting pairs of spins. For definiteness, we consider the case of a 2D square lattice with lattice constant a; however, results presented below remain valid for

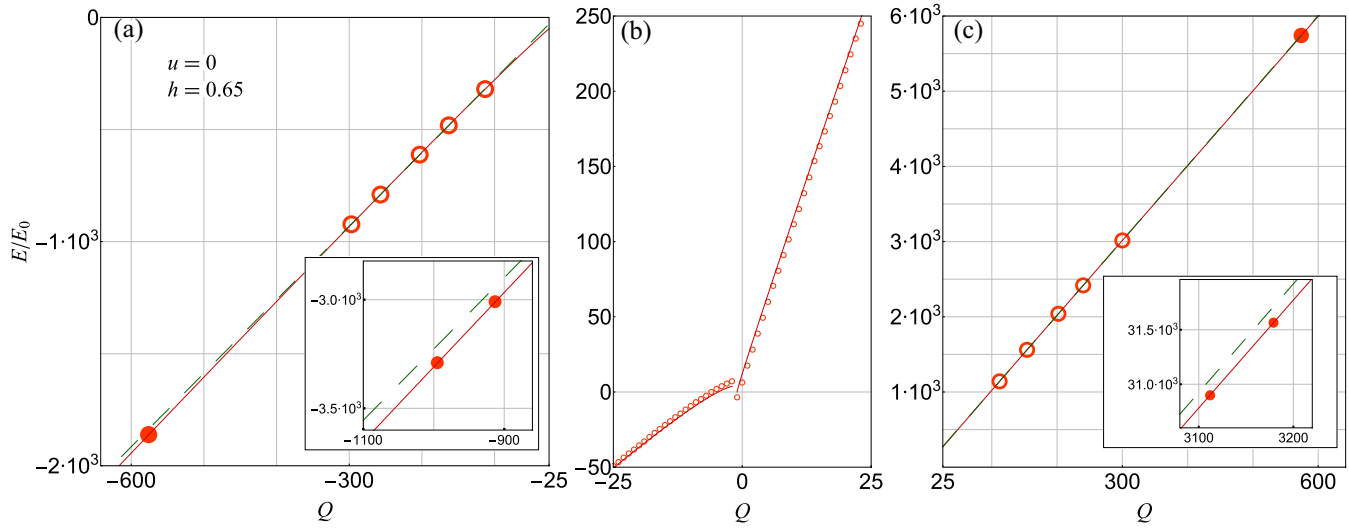

FIG. 6. The energy of skyrmions E as function of topological charge Q for: $Q \ll -1$ (a), $-25 \leqslant Q \leqslant 25$ (b), and $Q \gg 1$ (c). The solid curves are fit by (C1) for the points marked with empty circles in (a) and (c). The dashed lines in (a) and (c) are the linear fit for the same points. The solid circles in (a) and (c) and in the corresponding insets were not taken into account in the fitting process and are shown to illustrate a high quality of the fit obtained with Eq. (C1) and deviation of $E(Q)_{|Q|\gg 1}$ from the assumption of linear dependence.

other lattice symmetries as well. The dominant interaction in the system is the ferromagnetic exchange $0 < D < J$.

In the absence of uniaxial anisotropy and external magnetic field ($K_u = 0$, $B_{ext} = 0$) the ground state for (D1) is a spin spiral with a period $L = 2\pi a/\arctan(D/J)$ [91]. For $J \gg D$ (and therefore $L \gg a$) continuous limit (1) can be considered as a valid approximation for the lattice Hamiltonian (D1) with $\mathcal{A} = J/(2a)$, $\mathcal{D} = D/a^2$. The corresponding helix period $L_D = 2\pi aJ/D$. However, for $J \gtrsim D$ the continuum approach (1) representing a second-order Taylor expansion of the lattice model (D1) becomes invalid. For example, for $D = 0.6J$ the period L_D turns to be underestimated by about 10%. Thus, for such ratios between J and D the lattice effects are relevant.

For our simulations we used $J = 1.0$, $D = 0.6$. An important feature of skyrmions in the lattice model is the discrete degeneracy of the solutions, meaning that some in-plane directions are more preferable for texture alignment. In Figs. 7 and 8 we illustrate two possible skyrmion configurations for $Q = -2$ and $Q = 1$, respectively. The degree of degeneracy depends on the symmetry of the crystal lattice and on the morphology of the skyrmion spin texture. Note, the continuum model (1) is spatially isotropic and the energy of skyrmions does not depend on the orientation of the texture. For the calculation of topological charge on a discrete lattice we used the approach suggested in Ref. [92].

2. Chiral antiferromagnet

The spin-orbit interaction in antiferromagnets plays a similar role in the stabilization mechanism of skyrmions as in ferromagnetic mediums. Furthermore, the most realistic cases of a two-sublattice chiral antiferromagnet can be described in the frame of the same effective model as for a chiral ferromagnet [93,94].

For the simulation of antiferromagnets, we used a spin lattice Hamiltonian (D1) with $J = -1$, $D = 0.4$, $K_u = 0.22$, and $B_{ext} = 0$. In the corresponding phase diagram of a 2D chiral antiferromagnet, these parameters belong to the domain of confident stability of antiferromagnetic skyrmions [95].

For an antiferromagnet, in the absence of external magnetic field, the net magnetization reduces to zero. Therefore, it

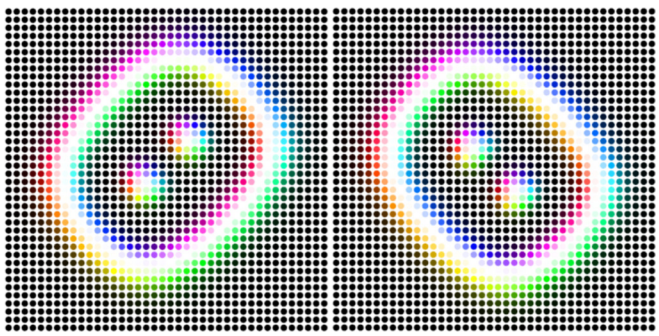

FIG. 7. Two energetically equivalent states for skyrmion with $Q = -2$ on a square lattice, for the case of zero magnetocrystalline anisotropy $K_u = 0$, $\mu_s B_{ext} = 0.25$.

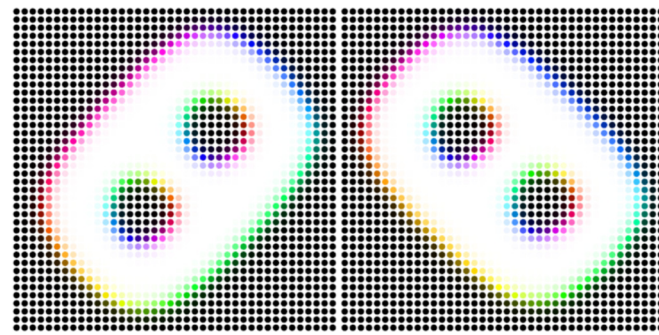

FIG. 8. Two energetically equivalent states for skyrmion with $Q = 1$ on a square lattice for the case of no external field $K_u = 0.45$, $\mu_s B_{ext} = 0$.

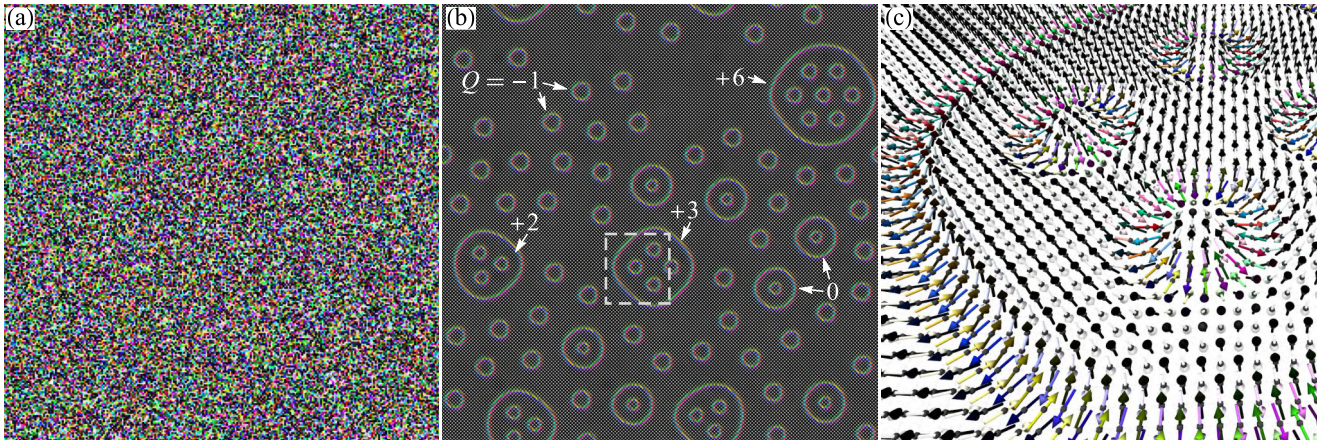

FIG. 9. The emergence of antiferromagnetic skyrmions with different topological charges as a result of full energy minimization starting from a random spins distribution. (a) The initial entirely random spins distribution with zero net magnetization, (b) the spin configuration after complete minimization, and (c) the perspective and zoomed view of the area marked in (b) as the dashed square. The color code is identical to that in all other images in the Appendixes and in the main text. Calculations have been performed on the domain with 256×256 spins and periodic boundary conditions in the plane. Texture with $Q = 0$ (antiferromagnetic skyrmionium) has been recently discussed in [98].

seems natural to use the configuration that meets this criterion as the initial state. Random spins distribution represent an inexhaustible set of initial states with a zero net magnetization. It turned out that such a simple initial guess with a regular probability leads to the appearance of skyrmions with various Q after direct energy minimization, see Fig. 9 and Supplemental Video 4 ("movie4_antiferromagnet.mp4"). The topological charge of an antiferromagnetic skyrmion can be calculated for either of the two sublattices and taking into account its polarity (net magnetization of sublattice). Because of the opposite polarities of the sublattices, the *superimposed* or *combined* winding number in this case always vanishes $-Q + Q = 0$. An important consequence of such vanishing of a winding number is the cancellation of so-called Magnus force – the force acting on topological magnetic soliton interacting with the spin-polarized electric current [96,97]. Note, cancellation of Magnus force is expected for any antiferromagnetic skyrmions irrespective of topological charge Q.

The feature of topological charge for an antiferromagnet can be illustrated using Fig. 9 as follows. Let us consider skyrmion with $Q = +3$ and three skyrmions with $Q = -1$ nearby. The total topological charge of such four textures is zero, which means that there is a way to merge these textures with further transformation into the ground state under preservation of the continuity in each of the sublattices.

[1] A. N. Bogdanov and D. A. Yablonskii, Sov. Phys. JETP **68**, 101 (1989).
[2] B. M. A. G. Piette, B. J. Schroers, and W. J. Zakrzewski, Z. Phys. C **65**, 165 (1995).
[3] T. Weidig, Nonlinearity **12**, 1489 (1999).
[4] J. Garaud, K. A. H. Sellin, J. Jäykkä, and E. Babaev, Phys. Rev. B **89**, 104508 (2014).
[5] T. H. R. Skyrme, Proc. R. Soc. London Sect. A **260**, 127 (1961).
[6] T. H. R. Skyrme, Nucl. Phys. **31**, 556 (1962).
[7] E. Babaev, L. D. Faddeev, and A. J. Niemi, Phys. Rev. B **65**, 100512(R) (2002).
[8] A. Bogdanov, JETP Lett. **62**, 247 (1995).
[9] R. Rajaraman, *Solitons and Instantons: An Introduction to Solitons and Instantons in Quantum Field Theory* (North-Holland, Amsterdam, 1982).
[10] X. Z. Yu, Y. Onose, N. Kanazawa, J. H. Park, J. H. Han, Y. Matsui, N. Nagaosa, and Y. Tokura, Nature (London) **465**, 901 (2010).
[11] N. Romming, C. Hanneken, M. Menzel, J. E. Bickel, B. Wolter, K. von Bergmann, A. Kubetzka, and R. Wiesendanger, Science **341**, 636 (2013).
[12] Y. Tokunaga, X. Z. Yu, J. S. White, H. M. Rønnow, D. Morikawa, Y. Taguchi, and Y. Tokura, Nat. Commun. **6**, 7638 (2015).
[13] I. Kézsmárki, S. Bordács, P. Milde, E. Neuber, L. M. Eng, J. S. White, H. M. Rønnow, C. D. Dewhurst, M. Mochizuki, K. Yanai, H. Nakamura, D. Ehlers, V. Tsurkan, and A. Loidl, Nat. Mater. **14**, 1116 (2015).
[14] A. K. Nayak, V. Kumar, T. Ma, P. Werner, E. Pippel, R. Sahoo, F. Damay, U. K. Rößler, C. Felser, and S. S. P. Parkin, Nature (London) **548**, 561 (2017).
[15] N. Kanazawa, S. Seki, and Y. Tokura, Adv. Mater. **29**, 1603227 (2017).
[16] C. Jin, Z.-A. Li, A. Kovács, J. Caron, F. Zheng, F. N. Rybakov, N. S. Kiselev, H. Du, S. Blügel, M. Tian, Y. Zhang, M. Farle, and R. E. Dunin-Borkowski, Nat. Commun. **8**, 15569 (2017).
[17] X. Z. Yu, N. Kanazawa, W. Z. Zhang, T. Nagai, T. Hara, K. Kimoto, Y. Matsui, Y. Onose, and Y. Tokura, Nat. Commun. **3**, 988 (2012).
[18] J. C. Loudon, A. O. Leonov, A. N. Bogdanov, M. C. Hatnean, and G. Balakrishnan, Phys. Rev. B **97**, 134403 (2018).

[19] H. Du, X. Zhao, F. N. Rybakov, A. B. Borisov, S. Wang, J. Tang, C. Jin, C. Wang, W. Wei, N. S. Kiselev, Y. Zhang, R. Che, S. Blügel, and M. Tian, Phys. Rev. Lett. **120**, 197203 (2018).

[20] N. S. Kiselev, A. N. Bogdanov, R. Schäfer, and U. K. Rößler, J. Phys. D: Appl. Phys. **44**, 392001 (2011).

[21] A. Fert, V. Cros, and J. Sampaio, Nat. Nanotech. **8**, 152 (2013).

[22] X. Zhang, M. Ezawa, and Y. Zhou, Sci. Rep. **5**, 9400 (2015).

[23] J. Müller, New J. Phys. **19**, 025002 (2017).

[24] F. Zheng, F. N. Rybakov, A. B. Borisov, D. Song, S. Wang, Z.-A. Li, H. Du, N. S. Kiselev, J. Caron, A. Kovács, M. Tian, Y. Zhang, S. Blügel, and R. E. Dunin-Borkowski, Nat. Nanotech. **13**, 451 (2018).

[25] P. F. Bessarab, G. P. Müller, I. S. Lobanov, F. N. Rybakov, N. S. Kiselev, H. Jónsson, V. M. Uzdin, S. Blügel, L. Bergqvist, and A. Delin, Sci. Rep. **8**, 3433 (2018).

[26] A. A. Belavin and A. M. Polyakov, JETP Lett. **22**, 245 (1975).

[27] A. O. Leonov and M. Mostovoy, Nat. Commun. **6**, 899 (2015).

[28] B. Dupé, C. N. Kruse, T. Dornheim, and S. Heinze, New J. Phys. **18**, 055015 (2016).

[29] S.-Z. Lin and S. Hayami, Phys. Rev. B **93**, 064430 (2016).

[30] L. Rózsa, K. Palotás, A. Deák, E. Simon, R. Yanes, L. Udvardi, L. Szunyogh, and U. Nowak, Phys. Rev. B **95**, 094423 (2017).

[31] T. Okubo, S. Chung, and H. Kawamura, Phys. Rev. Lett. **108**, 017206 (2012).

[32] N. Nagaosa and Y. Tokura, Nat. Nanotech. **8**, 899 (2016).

[33] A. Soumyanarayanan, N. Reyren, A. Fert, and C. Panagopoulos, Nature (London) **539**, 509 (2016).

[34] A. Fert, N. Reyren, and V. Cros, Nat. Rev. Mater. **2**, 17031 (2017).

[35] V. G. Bar'yakhtar and E. P. Stefanovsky, Fiz. Tverd. Tela **11**, 1946 (1969) [Sov. Phys. Solid State **11**, 1566 (1970)].

[36] P. Bak and M. H. Jensen, J. Phys. C: Solid State Phys. **13**, L881 (1980).

[37] I. Dzyaloshinsky, J. Phys. Chem. Solids **4**, 241 (1958).

[38] T. Moriya, Phys. Rev. **120**, 91 (1960).

[39] A. Bogdanov and A. Hubert, J. Magn. Magn. Mater. **195**, 182 (1999).

[40] J. Hagemeister, A. Siemens, L. Rózsa, E. Y. Vedmedenko, and R. Wiesendanger, Phys. Rev. B **97**, 174436 (2018).

[41] M. Finazzi, M. Savoini, A. R. Khorsand, A. Tsukamoto, A. Itoh, L. Duò, A. Kirilyuk, Th. Rasing, and M. Ezawa, Phys. Rev. Lett. **110**, 177205 (2013).

[42] S. Komineas and N. Papanicolaou, Phys. Rev. B **92**, 174405 (2015).

[43] M. Hoffmann, B. Zimmermann, G. P. Müller, D. Schürhoff, N. S. Kiselev, C. Melcher, and S. Blügel, Nat. Commun. **8**, 308 (2017).

[44] X. Zhang, Y. Zhou, and M. Ezawa, Phys. Rev. B **93**, 024415 (2016).

[45] W. Koshibae and N. Nagaosa, Nat. Commun. **7**, 10542 (2016).

[46] N. Romming, A. Kubetzka, C. Hanneken, K. von Bergmann, and R. Wiesendanger, Phys. Rev. Lett. **114**, 177203 (2015).

[47] X. Z. Yu, N. Kanazawa, Y. Onose, K. Kimoto, W. Z. Zhang, S. Ishiwata, Y. Matsui, and Y. Tokura, Nat. Mater. **10**, 106 (2011).

[48] X. Yu, A. Kikkawa, D. Morikawa, K. Shibata, Y. Tokunaga, Y. Taguchi, and Y. Tokura, Phys. Rev. B **91**, 054411 (2015).

[49] F. N. Rybakov, A. B. Borisov, and A. N. Bogdanov, Phys. Rev. B **87**, 094424 (2013).

[50] P. Milde, D. Köhler, J. Seidel, L. M. Eng, A. Bauer, A. Chacon, J. Kindervater, S. Mühlbauer, C. Pfleiderer, S. Buhrandt, C. Schütte, and A. Rosch, Science **340**, 1076 (2013).

[51] F. N. Rybakov, A. B. Borisov, S. Blügel, and N. S. Kiselev, Phys. Rev. Lett. **115**, 117201 (2015).

[52] A. O. Leonov, T. L. Monchesky, J. C. Loudon, and A. N. Bogdanov, J. Phys.: Condens. Matter **28**, 35LT01 (2016).

[53] F. Kagawa, H. Oike, W. Koshibae, A. Kikkawa, Y. Okamura, Y. Taguchi, N. Nagaosa, and Y. Tokura, Nat. Commun. **8**, 1332 (2017).

[54] F. N. Rybakov, A. B. Borisov, S. Blügel, and N. S. Kiselev, New J. Phys. **18**, 045002 (2016).

[55] W. Jiang, G. Chen, K. Liu, J. Zang, S. G. E. te Velthuis, and A. Hoffmann, Phys. Rep. **704**, 1 (2017).

[56] W. Jiang, P. Upadhyaya, W. Zhang, G. Yu, M. B. Jungfleisch, F. Y. Fradin, J. E. Pearson, Y. Tserkovnyak, K. L. Wang, O. Heinonen, S. G. E. te Velthuis, and A. Hoffmann, Science **349**, 283 (2015).

[57] O. Boulle, J. Vogel, H. Yang, S. Pizzini, D. de Souza Chaves, A. Locatelli, T. O. Menteş, A. Sala, L. D. Buda-Prejbeanu, O. Klein, M. Belmeguenai, Y. Roussigné, A. Stashkevich, S. M. Chérif, L. Aballe, M. Foerster, M. Chshiev, S. Auffret, I. M. Miron, and G. Gaudin, Nat. Nanotech. **11**, 449 (2016).

[58] S. Woo, K. Litzius, B. Krüger, M.-Y. Im, L. Caretta, K. Richter, M. Mann, A. Krone, R. M. Reeve, M. Weigand, P. Agrawal, I. Lemesh, M.-A. Mawass, P. Fischer, M. Kläui, and G. S. D. Beach, Nat. Mater. **15**, 501 (2016).

[59] S. McVitie, S. Hughes, K. Fallon, S. McFadzean, D. McGrouther, M. Krajnak, W. Legrand, D. Maccariello, S. Collin, K. Garcia, N. Reyren, V. Cros, A. Fert, K. Zeissler, and C. H. Marrows, Sci. Rep. **8**, 5703 (2018).

[60] A. H. Bobeck and E. Della Torre, *Magnetic Bubbles* (North-Holland, Amsterdam, 1975).

[61] I. E. Dzyaloshinskii, Sov. Phys. JETP **20**, 665 (1965).

[62] U. K. Rößler, A. A. Leonov, and A. N. Bogdanov, J. Phys.: Conf. Ser. **303**, 012105 (2011).

[63] C. Melcher, Proc. R. Soc. London Sect. A **470**, 20140394 (2014).

[64] A. O. Leonov, U. K. Rößler, and M. Mostovoy, Eur. Phys. J. Web Conf. **75**, 05002 (2014).

[65] X. Zhao, C. Jin, C. Wang, H. Du, J. Zang, M. Tian, R. Che, and Y. Zhang, Proc. Natl. Acad. Sci. USA **113**, 4918 (2016).

[66] J. Müller, J. Rajeswari, P. Huang, Y. Murooka, H. M. Rønnow, F. Carbone, and A. Rosch, Phys. Rev. Lett. **119**, 137201 (2017).

[67] W. Jiang, J. Xia, X. Zhang, Y. Song, C. Ma, H. Fangohr, G. Zhao, X. Liu, W. Zhao, and Y. Zhou, IEEE Magn. Lett. **9**, 3102905 (2018).

[68] W. Koshibae and N. Nagaosa, Sci. Rep. **8**, 6328 (2018).

[69] B. A. Ivanov, V. A. Stephanovich, and A. A. Zhmudskii, J. Magn. Magn. Mater. **88**, 116 (1990).

[70] X. Li and C. Melcher, J. Funct. Anal. **275**, 2817 (2018).

[71] C. Melcher, in *Lecture Notes of the 48th IFF Spring School 2017: Topological Matter – Topological Insulators, Skyrmions and Majoranas* (Forschungszentrum Jülich GmbH, 2017).

[72] See Supplemental Material at http://link.aps.org/supplemental/10.1103/PhysRevB.99.064437 for four video files and MuMax3 file.

[73] A. Bogdanov and A. Hubert, Phys. Status Solidi B **186**, 527 (1994).

[74] A. Bogdanov and A. Hubert, J. Magn. Magn. Mater. **138**, 255 (1994).
[75] O. A. Tretiakov and O. Tchernyshyov, Phys. Rev. B **75**, 012408 (2007).
[76] V. A. Galaktionov and J.-L. Vázquez, Discrete Contin. Dyn. Syst. **8**, 399 (2002).
[77] L. Rózsa, A. Deák, E. Simon, R. Yanes, L. Udvardi, L. Szunyogh, and U. Nowak, Phys. Rev. Lett. **117**, 157205 (2016).
[78] J. Garaud, J. Carlström, E. Babaev, and M. Speight, Phys. Rev. B **87**, 014507 (2013).
[79] Y. A. Kharkov, O. P. Sushkov, and M. Mostovoy, Phys. Rev. Lett. **119**, 207201 (2017).
[80] R. Wieser, R. Shindou, and X. C. Xie, Phys. Rev. B **95**, 064417 (2017).
[81] D. Foster, C. Kind, P. J. Ackerman, J.-S. B. Tai, M. R. Dennis, and I. I. Smalyukh, arXiv:1806.02576.
[82] A. Vansteenkiste, J. Leliaert, M. Dvornik, M. Helsen, F. Garcia-Sanchez, and B. V. Waeyenberge, AIP Adv. **4**, 107133 (2014).
[83] A. N. Bogdanov, M. V. Kudinov, and D. A. Yablonskii, Sov. Phys. Solid State **31**, 1707 (1989).
[84] A. S. Kovalev, A. M. Kosevich, and K. V. Maslov, JETP Lett. **30**, 296 (1980).
[85] V. P. Voronov, B. A. Ivanov, and A. M. Kosevich, Sov. Phys. JETP **57**, 1303 (1983).
[86] A. O. Leonov, T. L. Monchesky, N. Romming, A. Kubetzka, A. N. Bogdanov, and R. Wiesendanger, New J. Phys. **18**, 065003 (2016).
[87] S. Buhrandt and L. Fritz, Phys. Rev. B **88**, 195137 (2013).
[88] P. P. Horley, V. R. Vieira, P. D. Sacramento, and V. K. Dugaev, J. Phys. A: Math. Theor. **42**, 315211 (2009).
[89] P. E. Gill, M. Murray, and M. W. Wright, *Practical Optimization* (Academic, New York, 1981).
[90] I. A. Sergienko and E. Dagotto, Phys. Rev. B **73**, 094434 (2006).
[91] S. D. Yi, S. Onoda, N. Nagaosa, and J. H. Han, Phys. Rev. B **80**, 054416 (2009).
[92] B. Berg and M. Lüscher, Nucl. Phys. B **190**, 412 (1981).
[93] A. Bogdanov and A. Shestakov, Phys. Solid State **40**, 1350 (1998).
[94] A. N. Bogdanov, U. K. Rößler, M. Wolf, and K.-H. Müller, Phys. Rev. B **66**, 214410 (2002).
[95] P. F. Bessarab, D. Yudin, D. R. Gulevich, P. Wadley, M. Titov, and O. A. Tretiakov, arXiv:1709.04454.
[96] X. Zhang, Y. Zhou, and M. Ezawa, Sci. Rep. **6**, 24795 (2016).
[97] J. Barker and O. A. Tretiakov, Phys. Rev. Lett. **116**, 147203 (2016).
[98] M. M. M. Bhukta, A. Mishra, G. Pradhan, S. Mallick, B. B. Singh, and S. Bedanta, arXiv:1810.08262.